# ARTICLE

# Cooperative insertion of $CO_2$ in diamine–appended metal–organic frameworks

Thomas M. McDonald[1], Jarad A. Mason[1], Xueqian Kong[2,3], Eric D. Bloch[1], David Gygi[1], Alessandro Dani[4], Valentina Crocellà[4], Filippo Giordanino[4], Samuel O. Odoh[5], Walter S. Drisdell[6], Bess Vlaisavljevich[2], Allison L. Dzubak[5], Roberta Poloni[7,8], Sondre K. Schnell[2,9], Nora Planas[5], Kyuho Lee[2,10], Tod Pascal[10], Liwen F. Wan[10], David Prendergast[10], Jeffrey B. Neaton[10,11,12], Berend Smit[2,6,13], Jeffrey B. Kortright[6], Laura Gagliardi[5], Silvia Bordiga[4], Jeffrey A. Reimer[2,6] & Jeffrey R. Long[1,6]

The process of carbon capture and sequestration has been proposed as a method of mitigating the build-up of greenhouse gases in the atmosphere. If implemented, the cost of electricity generated by a fossil fuel-burning power plant would rise substantially, owing to the expense of removing $CO_2$ from the effluent stream. There is therefore an urgent need for more efficient gas separation technologies, such as those potentially offered by advanced solid adsorbents. Here we show that diamine-appended metal-organic frameworks can behave as 'phase-change' adsorbents, with unusual step-shaped $CO_2$ adsorption isotherms that shift markedly with temperature. Results from spectroscopic, diffraction and computational studies show that the origin of the sharp adsorption step is an unprecedented cooperative process in which, above a metal-dependent threshold pressure, $CO_2$ molecules insert into metal-amine bonds, inducing a reorganization of the amines into well-ordered chains of ammonium carbamate. As a consequence, large $CO_2$ separation capacities can be achieved with small temperature swings, and regeneration energies appreciably lower than achievable with state-of-the-art aqueous amine solutions become feasible. The results provide a mechanistic framework for designing highly efficient adsorbents for removing $CO_2$ from various gas mixtures, and yield insights into the conservation of $Mg^{2+}$ within the ribulose-1,5-bisphosphate carboxylase/oxygenase family of enzymes.

Exceeding 13 gigatonnes (Gt) annually[1], carbon dioxide generated from the combustion of fossil fuels for the production of heat and electricity is a major contributor to climate change and ocean acidification[2,3]. Implementation of carbon capture and sequestration technologies has been proposed as a means of enabling the continued use of fossil fuels in the short term, while renewable energy sources gradually replace our existing infrastructure[4]. The removal of $CO_2$ from low-pressure flue gas mixtures is currently effected by aqueous amine solutions that are highly selective for acid gases[5]. As a result of the large energy penalty for desorbing $CO_2$ from such liquids, solid adsorbents with appreciably lower heat capacities are frequently proposed as promising alternatives[6,7]. In particular, as a result of their high surface areas and tunable pore chemistry, the separation capabilities of certain metal-organic frameworks have been shown to meet or exceed those achievable by zeolite or carbon adsorbents[8–10].

Recently, the attachment of alkyldiamines to coordinatively unsaturated metal sites lining the pores of selected metal-organic frameworks has been demonstrated as a simple methodology for increasing low-pressure $CO_2$ adsorption selectivity and capacity[11–14]. Most notably, functionalization of $Mg_2(dobpdc)$ ($dobpdc^{4-} = 4,4'$-dioxidobiphenyl-3,3'-dicarboxylate), an expanded variant of the well-studied metal-organic framework $Mg_2(dobdc)$ ($dobdc^{4-} = 2,5$-dioxidobenzene-1,4-dicarboxylate)[15–18], with $N,N'$-dimethylethylenediamine (mmen) generated an adsorbent with exceptional $CO_2$ capacity under flue gas conditions and unusual, unexplained step-shaped adsorption isotherms[13]. Here we elucidate the unprecedented mechanism giving rise to these step-shaped isotherms and demonstrate that replacing $Mg^{2+}$ with other divalent metal ions enables the position of the $CO_2$ adsorption step to be manipulated in accord with the metal-amine bond strength. As we will show, the resulting mmen-$M_2(dobpdc)$ (M = Mg, Mn, Fe, Co, Zn) compounds, here designated 'phase-change' adsorbents, can have highly desirable characteristics that make them superior to other solid or liquid sorbents for the efficient capture of $CO_2$.

Figure 1 illustrates the extraordinary advantages associated with using an adsorbent exhibiting step-shaped isotherms in a temperature swing adsorption process in comparison with the Langmuir-type isotherms observed for most microporous adsorbents. For carbon capture applications, a gas mixture containing $CO_2$ at low pressure ($P_{ads}$) and low temperature ($T_{low}$) is contacted with the adsorbent, which selectively adsorbs a large amount of $CO_2$. The adsorbent is heated to liberate pure $CO_2$ with a partial pressure of $P_{des}$, and is then reused for subsequent adsorption–desorption cycles. For a classical adsorbent (Fig. 1a), including all previous amine-based sorbents, the steepness of the isotherm gradually diminishes as the temperature increases, necessitating a high desorption temperature to achieve a large working capacity for a separation. In contrast, for a phase-change adsorbent of the type investigated here (Fig. 1b), the position of the isotherm step shifts markedly to higher pressures as the temperature increases, such that a large working capacity can be achieved with only a small increase in temperature. For an efficient carbon capture process, one would ideally create a phase-change

[1]Department of Chemistry, University of California, Berkeley, California 94720, USA. [2]Department of Chemical and Biological Engineering, University of California, Berkeley, California 94720, USA. [3]Department of Chemistry, Zhejiang University, Hangzhou 310027, China. [4]Chemistry Department, NIS and INSTM Centre of Reference, University of Turin, Via Quarello 15, I-10135 Torino, Italy. [5]Department of Chemistry, Chemical Theory Center and Supercomputing Institute, University of Minnesota, Minneapolis, Minnesota 55455, USA. [6]Materials Sciences Division, Lawrence Berkeley National Laboratory, Berkeley, California 94720, USA. [7]Université Grenoble Alpes, Science et Ingénierie des Matériaux et Procédés (SIMAP), F-38000 Grenoble, France. [8]Centre National de la Recherche Scientifique, SIMAP, F-38000, Grenoble, France. [9]Department of Chemistry, Norwegian University of Science and Technology, Høgskoleringen 5, 7491 Trondheim, Norway. [10]Molecular Foundry, Lawrence Berkeley National Laboratory, One Cyclotron Road, Berkeley, California 94720, USA. [11]Department of Physics, University of California, Berkeley, California 94720, USA. [12]Kavli Energy Nanosciences Institute, University of California, Berkeley, California 94720, USA. [13]Institut des Sciences et Ingénierie Chimiques, Valais, École Polytechnique Fédérale de Lausanne (EPFL), Rue de l'Industrie 17, CH-1950 Sion, Switzerland.
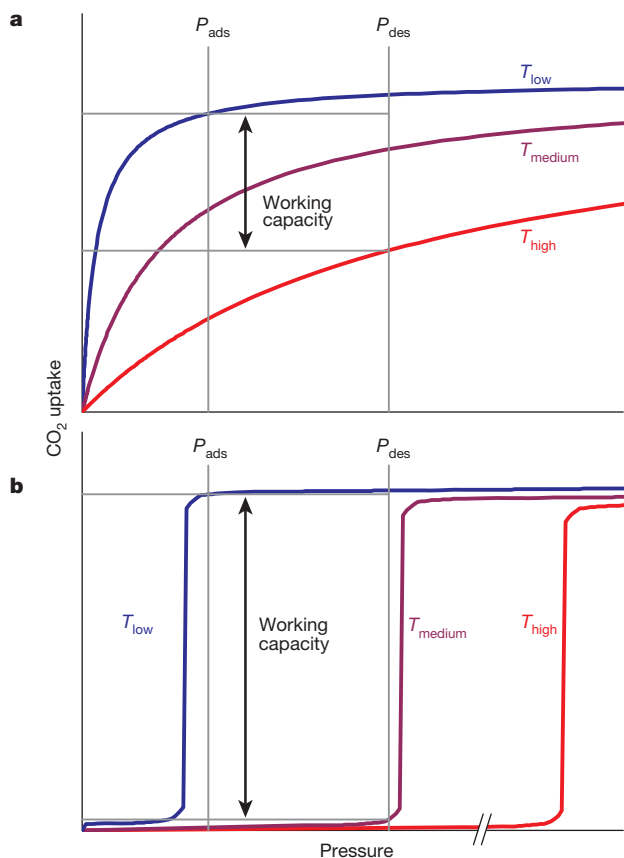
**Figure 1 | Idealized $CO_2$ adsorption isotherms.** Variation in the idealized adsorption isotherm behaviour with temperature for a classical microporous adsorbent (**a**), showing the usual Langmuir-type isotherm shape, compared with that of a phase-change adsorbent (**b**), showing step-shaped (sometimes referred to as 'S-shaped') isotherms. The double-headed black arrow indicates the working capacity (that is, the amount of gas removed) for a separation performed using a temperature swing adsorption process in which selective adsorption occurs at $P_{ads}$ and $T_{low}$ and desorption is performed at $P_{des}$ and $T_{high}$ (**a**) or $T_{medium}$ (**b**).

adsorbent with a large vertical step positioned below the partial pressure of $CO_2$ in the flue gas.

## Cooperative insertion of $CO_2$ into metal–amine bonds

Spectroscopic and diffraction measurements were undertaken to determine the mechanism of $CO_2$ uptake leading to a steep adsorption step for adsorbents such as mmen-$Mg_2$(dobpdc). In particular, powder X-ray diffraction studies, which were performed on the isostructural compound mmen-$Mn_2$(dobpdc) owing to the greater crystallinity of its base framework, provided detailed structural information on how $CO_2$ binds within the channels of the material. Diffraction data collected at 100 K before and after exposure of a sample to 5 mbar of $CO_2$ showed the unit cell volume contracting by just 1.112(8)%, but revealed large changes in the relative intensity of selected diffraction peaks (Fig. 2a). Complete structural models were developed for both data sets using the simulated annealing method, as implemented in TOPAS-Academic[19], followed by Rietveld refinement against the data (Fig. 3, Extended Data Fig. 1 and Supplementary Tables 1–4). Before exposure to $CO_2$, the mmen molecules were bound through one amine group to the $Mn^{2+}$ sites with a Mn–N distance of 2.29(6) Å, whereas the other amine lay exposed on the surface of the framework (Fig. 3c). Counter to our initial assumption that the uncoordinated amine groups would serve to bind $CO_2$ (refs 13, 20), $CO_2$ adsorption instead occurred by means of full insertion into the Mn–N bond, resulting in a carbamate with one O atom bound to Mn at a distance of 2.10(2) Å (Fig. 3d). The second O atom of the carbamate
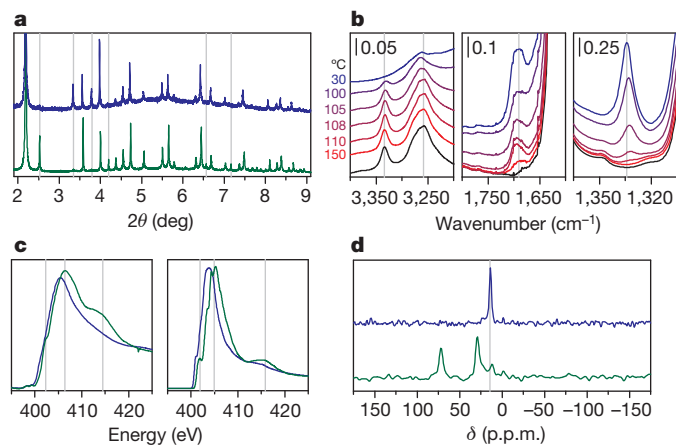
**Figure 2 | Experimental characterization of the adsorption mechanism. a**, Large intensity differences are apparent in the powder X-ray diffraction patterns (collected at 100 K) on exposure of mmen-$Mn_2$(dobpdc) (blue) to 5 mbar $CO_2$ (green). **b**, Infrared spectra on dosing an activated sample of mmen-$Mg_2$(dobpdc) (black) with $CO_2$ and cooling from 150 °C to 30 °C (red to blue) under 5% $CO_2$ in $N_2$. The three different regions show bands corresponding to N–H (left), C–O (centre) and C–N (right) stretching vibrations. Spectra in the left panel are artificially offset by 0.05 a.u. to aid in visualization. Those in the other two panels are not offset; there $CO_2$ adsorption is responsible for the increase in the spectral baseline due to molecular charge delocalization of the ammonium carbamate chains. **c**, Experimental (left) and computational (right) NEXAFS spectra of mmen-$Mg_2$(dobpdc) at the N K-edge, before (blue) and after (green) $CO_2$ adsorption; the three major spectral changes are reproduced. **d**, Solid-state $^{15}N$ NMR spectra for mmen-$Mg_2$(dobpdc) before (blue) and after (green) exposure to $CO_2$ at 25 °C.

had a close interaction of 2.61(9) Å with the N atom of a neighbouring mmen, resulting in chains of ammonium carbamate running along the crystallographic *c* axis of the structure (Fig. 3e). The observed ammonium carbamate N···O distance was similar to the distance of 2.66–2.72 Å in a single crystal of pure mmen-$CO_2$ (methyl(2-(methylammonio) ethyl)carbamate)[21]. This well-ordered chain structure was maintained at 295 K, as determined from a full Rietveld refinement against data collected at this temperature. Thus, the adsorption of $CO_2$ at ambient temperatures is associated with a structural transition to form an extended chain structure held together by ion pairing between the metal-bound carbamate units and the outstretched ammonium group of a neighbouring mmen molecule.

The foregoing structural information enabled the formulation of a detailed mechanism for the adsorption of $CO_2$ in phase-change adsorbents of the type mmen-$M_2$(dobpdc). As shown in Fig. 4, the uncoordinated amine of a mmen molecule acts as a strong base to remove the acidic proton from the metal-bound amine of a neighbouring mmen molecule. Deprotonation occurs only in the presence of $CO_2$, such that simultaneous nucleophilic addition of $CO_2$ results in the formation of a carbamate with an associated ammonium countercation. At suitable temperatures and pressures, rearrangement of the carbamate is possible such that the M–N bond is broken and a M–O bond is formed. Critically, the ion-pairing interaction causes the mmen molecule to stretch, destabilizing the M–N bond and facilitating insertion at the next metal site. This cooperative effect will propagate until a complete one-dimensional ammonium carbamate chain has formed. Indeed, it is this cooperativity that leads to the sudden uptake of a large amount of $CO_2$ and a steep vertical step in the adsorption isotherm.

Infrared spectroscopy measurements performed on mmen-$Mg_2$(dobpdc) fully support the proposed mechanism. As shown in Fig. 2b, changes to the infrared spectrum were apparent when a sample of the compound was cooled isobarically from 150 °C to 30 °C at 1 °C $min^{-1}$ under flowing 5% $CO_2$ in a $N_2$ atmosphere. At high temperatures, two distinct N–H vibrations arose at 3,258 and 3,334 $cm^{-1}$, which were also present in the spectrum of mmen-$Mg_2$(dobpdc) in the
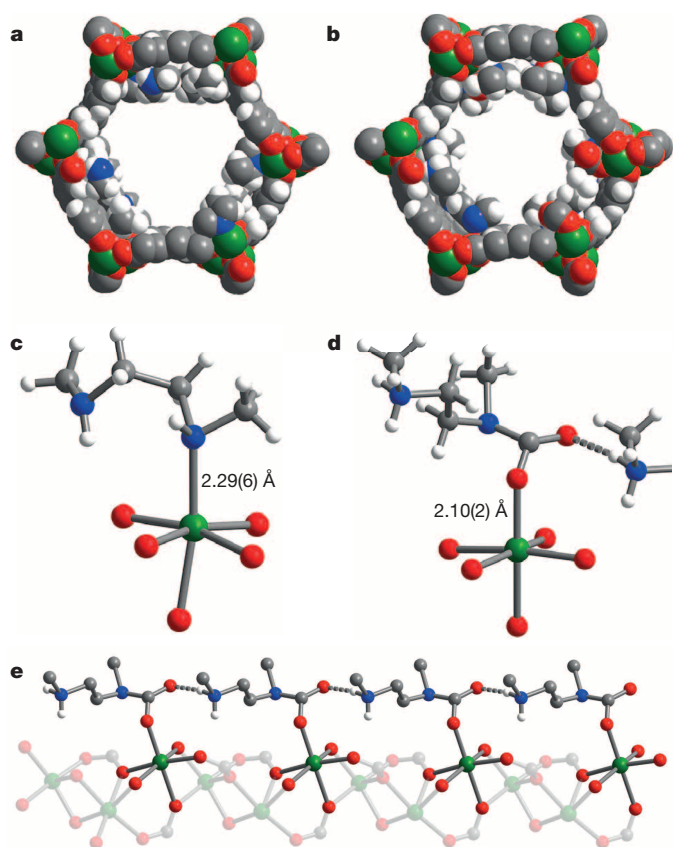
**Figure 3 | Powder X-ray diffraction structures of mmen-Mn₂(dobpdc).**
**a, b,** Space-filling models of the solid-state structures of mmen-Mn₂(dobpdc)
(**a**) and $CO_2$-mmen-Mn₂(dobpdc) (**b**) at 100 K. **c, d,** Portions of the
crystal structures for mmen-Mn₂(dobpdc) before (**c**) and after (**d**) $CO_2$
adsorption, as determined from powder X-ray diffraction data. **e,** A portion of the
crystal structure for the final configuration of $CO_2$ adsorbed within mmen-
Mn₂(dobpdc), depicting the formation of an ammonium carbamate chain along
the pore surface. Green, grey, red, blue and white spheres represent Mn, C, O, N
and H atoms, respectively; some H atoms are omitted for clarity.



**Figure 4 | A cooperative insertion mechanism for $CO_2$ adsorption.** Depiction
of the mechanism for $CO_2$ adsorption at four neighbouring M–mmen sites
within an infinite one-dimensional chain of such sites running along the
crystallographic *c* axis of a mmen-M₂(dobpdc) compound. Simultaneous
proton transfer and nucleophilic attack of N on a $CO_2$ molecule forms
an ammonium carbamate species that destabilizes the amine coordinated
at the next metal site, initiating the cooperative adsorption of $CO_2$ by a
chain reaction.

absence of $CO_2$ and could be attributed to the coordinated and unco-
ordinated ends of mmen, respectively. On cooling, both of these N–H
resonances disappeared, indicating changes to both amines of mmen,
while a new, extremely broad N–H band characteristic of ammonium
formation appeared. From the weak but clearly discernible C=O vibra-
tion at $1,690\ cm^{-1}$, carbamate formation between mmen and $CO_2$ oc-
curred under all conditions, even at high temperatures. However, an
additional sharp band at $1,334\ cm^{-1}$, corresponding to the C–N vibra-
tional mode of a carbamate, was observed only on cooling below 110 °C.
The delayed onset of this easily recognizable band, which is diagnostic
of a phase-change adsorbent of the type investigated here, is attributable
to changes in the resonance configuration of carbamate that occur on
coordination of one of its O atoms. The normalized intensities of the
C–N band and a second band at $658\ cm^{-1}$ versus temperature dem-
onstrate that their formation was directly related to the sharp step in the
gravimetric adsorption isobar measured under identical experimental
conditions. From the infrared spectra it is clear that although a small
amount of $CO_2$ can be adsorbed by means of ammonium carbamate
formation between pairs of adjacent amines, it is specifically the adsorp-
tion of $CO_2$ to form ammonium carbamate chains that endows these
materials with their step-change adsorption properties (see Extended
Data Fig. 2 for additional infrared spectra).

To better understand the stepwise pathway by which the amines ini-
tially adsorb $CO_2$, density functional theory (DFT) calculations were
paired with *in situ* near-edge X-ray absorption fine structure (NEXAFS)
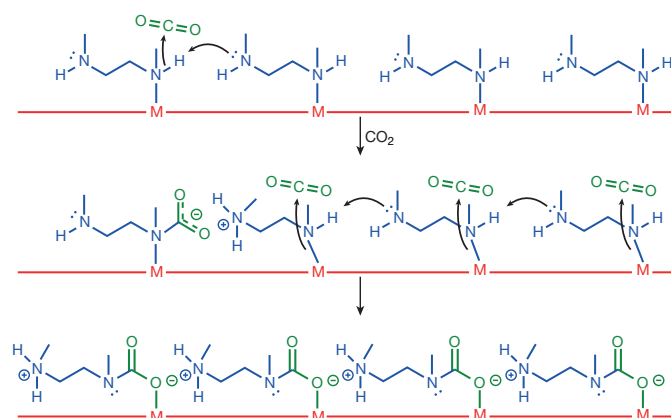measurements of the nitrogen K-edge of mmen-Mg₂(dobpdc) collected
under increasing $CO_2$ pressure (Fig. 2c and Extended Data Fig. 3)[22], and
all observed spectral changes were accurately reproduced by computed
spectra. From the NEXAFS spectra, the new pre-edge peak at 402.3 eV
arose solely from the carbamate nitrogen and was a clear signature of
carbamate insertion into the metal–nitrogen bond. As in infrared spec-
troscopy, this feature is attributable to resonance of the nitrogen lone
pair into the π system of the carbamate after the breaking of the coord-
inate bond using the same electron pair with the Mg metal centre. A
second new, broad feature between 411 and 419 eV also arose solely
from the carbamate nitrogen and was a signature of the new N–C bond
formed on adsorption of $CO_2$. This feature appeared before insertion
and was general to both terminal-bound and inserted carbamate moi-
eties. Finally, the ∼1 eV blueshift of the main edge peak at 405.4 eV was
characteristic of ammonium formation.

Solid-state NMR spectra indicated that $CO_2$ adsorption affected the
manner in which diamines were coordinated to the metal sites of the
framework (Fig. 2d). On exposure of mmen-Mg₂(dobpdc) to $CO_2$, ¹⁵N
chemical shifts consistent with ammonium and carbamate were observed
at 31 and 72 p.p.m., respectively. Yet only a single ¹⁵N resonance was
apparent for mmen-Mg₂(dobpdc) in the absence of $CO_2$. This indicates
that the coordinated and uncoordinated ends of the mmen molecules
were capable of interconverting on the timescale of the NMR experi-
ment, although, as discussed above, they were distinguishable on the
much faster timescale of infrared spectroscopy. Despite being labile, the
amines were stable to evacuation under vacuum at high temperatures.
This unexpected lability seems to allow substitution, but not elimina-
tion, reactions to occur rapidly under conditions relevant to carbon
capture. Furthermore, the sudden adsorption of $CO_2$ in this compound
is thus associated with a transition from a dynamic surface state to a
well-ordered extended surface structure. Accordingly, the reaction with
$CO_2$ can be considered to be thermodynamically non-spontaneous at
low pressures because of the large decrease in entropy associated with
this transition. Indeed, the molar entropy of gas-phase $CO_2$ was found
to be the primary determinant of the step pressure for phase-change
adsorbents. As shown in Extended Data Fig. 4, step pressures for all five
phase-change metal organic frameworks were linearly correlated with
the gas-phase entropy of $CO_2$ as a function of temperature.

## Understanding and manipulating the isotherm steps

The mechanism of $CO_2$ adsorption suggests that variation of the metal-
amine bond strength should provide a method of manipulating the

isotherm step position. The series of isostructural compounds mmen-$M_2$(dobpdc) (M = Mg, Mn, Fe, Co, Ni, Zn) were therefore synthesized, and the $CO_2$ adsorption isotherms for each were measured at 25, 40, 50 and 75 °C (Fig. 5). With the exception of the Ni compound, which showed normal Langmuir-type adsorption behaviour (Fig. 5e), all of the materials showed sharp isotherm steps that shifted to higher pressure with increasing temperature. Analysis of the isotherm steps at 25 °C yielded Hill coefficients[23] of 10.6, 5.6, 7.5, 11.5 and 6.0 for M = Mg, Mn, Fe, Co and Zn, respectively, reflecting the cooperative nature of the $CO_2$ adsorption mechanism. Simulated isotherms generated from grand-canonical Monte Carlo simulations using a simple lattice model captured the experimentally observed isotherm step only when all mmen groups reacted with $CO_2$ and aligned down the crystallographic $c$ axis (see Extended Data Fig. 5).

For a given temperature, the step position varies in the order Mg < Mn < Fe < Zn < Co, in good agreement with the published series for octahedral metal complex stabilities[24]. The lack of a step for the Ni compound, even at very high pressures (Extended Data Fig. 6) is attributable to the exceptional stability of the Ni–mmen bond, which prevents carbamate insertion from taking place under the conditions surveyed. Geometry optimizations performed with periodic DFT calculations[25] using various functionals were in good agreement with experimentally calculated values, and the trend in the calculated adsorption energies was directly correlated with the calculated metal-amine bond length (Extended Data Fig. 5). Thus, we predict that similar variations in tuning step position will be possible for the $M_2$(dobpdc) series by altering the sterics of the amine bound to the metal, as well as the spacer between the two amine groups. Hence, depending on the concentration of $CO_2$

present in a gas mixture, an adsorbent can be rationally designed to match the optimum process conditions depicted in Fig. 1.

Although stepped adsorption isotherms[26] have been observed previously in solid adsorbents, the origin of the step reported here is unique and distinct from all previously reported mechanisms. First, in contrast to most metal-organic frameworks showing such behaviour, the isotherm steps reported here are not attributable to pore-opening, gate-opening or pore-closing processes[27–29]. For mmen-$Mn_2$(dobpdc), only a ~1% decrease in the unit cell volume was observed on $CO_2$ adsorption, and from Fig. 3a, b it is apparent that the entire pore surface was accessible to $CO_2$ throughout the adsorption isotherm. A gate-opening mechanism attributable to the rearrangement of flexible hydrogen-bonding functional groups, which function by preventing $CO_2$ diffusion into the pores at low partial pressures[30], cannot explain the presence of distinct adsorption steps when the material is slowly cooled from high to low temperatures under isobaric adsorption conditions (see below). Second, in contrast to adsorbed-layer phase transitions on highly homogeneous surfaces, the adsorbed phase reported here was stable at temperatures well above the critical temperature of $CO_2$ (ref. 31). Third, the phase transition was a metal cation-dependent, solid-to-solid transformation, in contrast to liquid-to-liquid or liquid-to-solid phase change reactions typically reported for amine–$CO_2$ systems[32–34]. Last, under conditions relevant to $CO_2$ capture, desorption hysteresis was minimal, because the sharp steps occurred over a narrow pressure regime and the adsorption and desorption onset points were at about the same temperature and pressure (see Extended Data Fig. 7).

Several features unique to the mmen-$M_2$(dobpdc) series permitted phase transitions of this type to be observed. First, for solid ammonium carbamate chains to form, the metal-amine coordinate bond must be capable of rearrangement. Thus, only amines tethered to the solid surface through coordinate bonds rather than covalent bonds can undergo the mechanism reported here. Second, a homogeneous surface with appropriately positioned adsorption sites, which is dictated by the location of open metal sites within the pores of the metal-organic framework, is necessary. Thus, a very limited number of metal-organic framework materials would be able to mimic the adsorption behaviour reported here, and it is likely that no amine-functionalized mesoporous silica sorbent could be engineered precisely enough to meet these requirements. Notably, in contrast to the pore expanded derivatives of $M_2$(dobdc) reported here, amine functionalization of the parent $Mg_2$(dobdc) compound was not reported to result in stepped adsorption isotherms[35].

## Low–energy carbon capture applications

Effective adsorbents for carbon capture must possess large working capacities for processes occurring at temperatures above 40 °C and at $CO_2$ partial pressures near 0.15 bar for coal flue gas or near 0.05 bar for a natural gas flue stream. On this basis, the location of the isotherm steps for the Mg and Mn compounds makes them better suited for this application than the Fe, Co or Zn compounds, which are better suited for separations from gas mixtures with higher $CO_2$ concentrations. To assess the utility of these phase-change adsorbents for capturing $CO_2$ in a pure temperature swing adsorption process, adsorption isobars were collected under dynamic gas flow. Samples of mmen-$Mg_2$(dobpdc) and mmen-$Mn_2$(dobpdc) were activated, saturated with 100% $CO_2$ and then cooled isobarically to room temperature under three different $CO_2$-containing gas mixtures: 100%, 15% and 5%. The resulting isobars, shown in Fig. 6a, b, reveal how small changes in temperature induced large changes in the quantity of $CO_2$ adsorbed. As shown in Fig. 6c, d, phase-change adsorbents showed very large working capacities when used in temperature swing adsorption processes. For mmen-$Mg_2$(dobpdc) to give a working capacity in excess of 13 wt%, the material must simply swing between 100 and 150 °C. Similarly, the working capacity of mmen-$Mn_2$(dobpdc) was in excess of 10 wt% when cycled between 70 and 120 °C. In particular, to simulate a pure temperature swing adsorption process accurately, 15% $CO_2$ in $N_2$ was flowed over the samples during the cooling phase, whereas 100% $CO_2$ was used during heating phases.
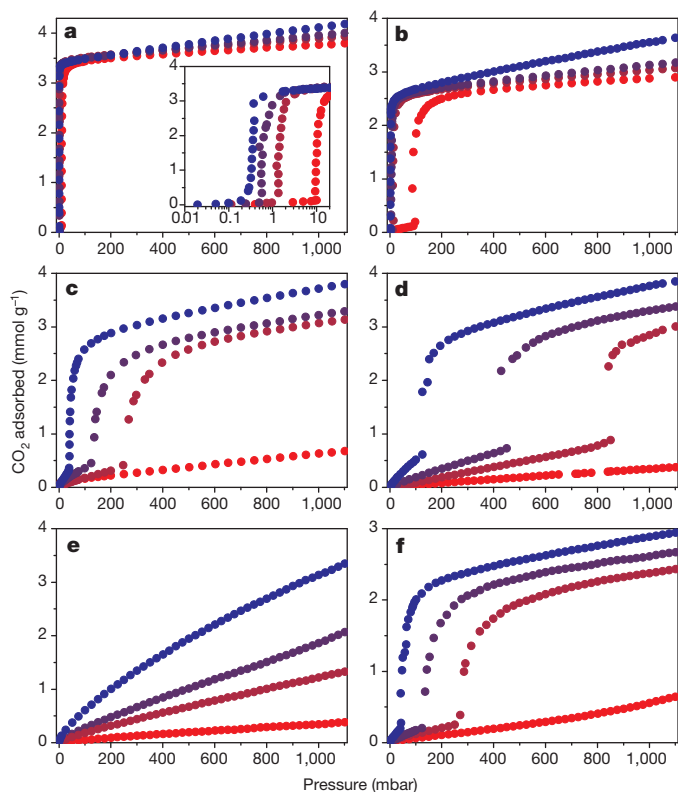


**Figure 5 | $CO_2$ adsorption isotherms.** Carbon dioxide adsorption isotherms at 25 °C (blue), 40 °C (blue-violet), 50 °C (red-violet) and 75 °C (red) for mmen-$Mg_2$(dobpdc) (**a**), mmen-$Mn_2$(dobpdc) (**b**), mmen-$Fe_2$(dobpdc) (**c**), mmen-$Co_2$(dobpdc) (**d**), mmen-$Ni_2$(dobpdc) (**e**) and mmen-$Zn_2$(dobpdc) (**f**). Despite the use of aliphatic amine groups as the $CO_2$ reactive species, the metal-organic framework has an essential role in determining isotherm shape, owing to the importance of metal–ligand reorganization reactions in the mechanism.
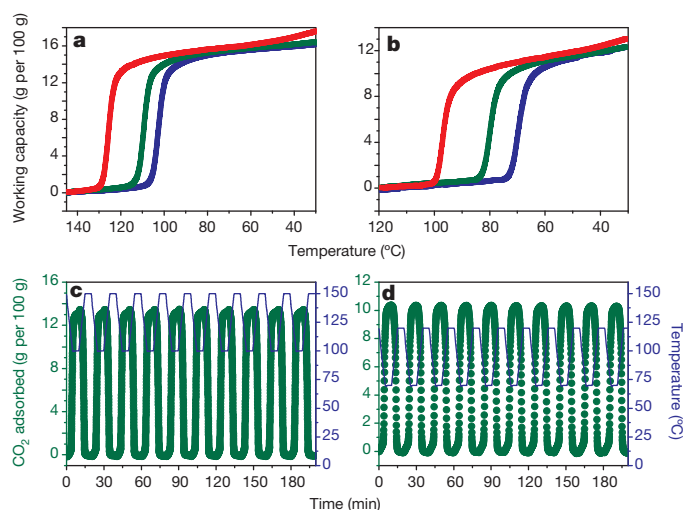
**Figure 6 | Isobaric CO₂ adsorption and cycling experiments. a, b,** Variable-temperature adsorption isobars of 100% (red), 15% (green) and 5% (blue) CO₂ (in N₂) for mmen-Mg₂(dobpdc) (**a**) and mmen-Mn₂(dobpdc) (**b**), showing that under dynamic conditions the sharp transition region allows phase-change adsorbents to achieve very large working capacities under a wide range of adsorption conditions. For each material, the phase-transition temperature is dependent on the pressure of CO₂ in the gas mixture, with higher phase-transition temperatures being observed at higher CO₂ partial pressures. **c, d,** Cycling data for a pure temperature swing process involving adsorption from a simulated coal flue gas (15% CO₂ in N₂) at 100 °C in mmen-Mg₂(dobpdc) (**c**) and 70 °C in mmen-Mn₂(dobpdc) (**d**), followed by desorption at 150 and 120 °C, respectively, using a flow of 100% CO₂. Respective working capacities of 13% and 10% are attained, with no loss in capacity over the course of ten cycles.

In contrast to experiments that use a purge gas to assist CO₂ desorption, no inert gases were used to regenerate the samples.

Estimations based on differential scanning calorimetry, thermogravimetric analysis and isosteric heat determinations indicate that mmen-Mg₂(dobpdc) and mmen-Mn₂(dobpdc) can achieve regeneration energies of about 2.2–2.3 MJ per kg of CO₂ captured. This value is appreciably lower than the regeneration energies attainable using monoethanolamine (3.5 MJ kg⁻¹) or even state-of-the-art amines, such as piperazine and KS-1 (2.6 MJ kg⁻¹)[5,36]. In contrast to aqueous amine absorbents that use heat exchangers to save sensible energy costs, the greater working capacities and smaller temperature swings of phase-change adsorbents allow more economical processes to be developed for a high-enthalpy adsorbent without the use of a heat exchanger. Because phase-change adsorbents saturate with CO₂ at their transition point, it is not necessary for adsorption to occur at the lowest possible temperature. Whereas we previously showed that mmen-Mg₂(dobpdc) can operate effectively under standard flue gas adsorption conditions (40 °C)[13], Fig. 6 shows that phase-change adsorbents operated more efficiently at higher adsorption temperatures than at lower temperatures. Because classical adsorbents must operate at the lowest possible adsorption temperature to maximize working capacity, only phase-change adsorbents can enable high-temperature adsorption processes to be considered.

Adsorbing CO₂ at elevated temperatures affords several additional process benefits besides directly decreasing sorbent regeneration energy. In particular, overcoming the competitive adsorption of water vapour, which is present in flue gas at high concentrations, presents a serious challenge for solid adsorbents. Amine-based solid adsorbents fare better than those using a purely physical adsorption mechanism, because they are known to retain their affinity for CO₂ under humid conditions[37], as also shown here for mmen-Mg₂(dobpdc) (see Extended Data Fig. 7 for additional dynamic gas adsorption experiments). However, even for systems where the amine reactivity with CO₂ is unaffected by the presence of water, the physical adsorption of water on non-amine

binding sites increases the overall regeneration energy of the material[38]. As shown in Extended Data Fig. 6b, mmen-Mg₂(dobpdc) adsorbed nearly 90% less water at 100 °C than at 40 °C. Thus, the energy penalty associated with desorbing co-adsorbed water can be substantially decreased by performing CO₂ adsorption at a high temperature, obviating the need for strict flue gas dehumidification. No changes to the CO₂ adsorption isotherm were apparent after exposure to water at 40 or 100 °C, indicating the stability of the mmen-Mg₂(dobpdc) in the presence of water vapour even at high temperatures.

The high effective operating temperatures of mmen-Mg₂(dobpdc) and mmen-Mn₂(dobpdc) offer opportunities for cost savings beyond just decreases in the regeneration energy. Because of the exothermic nature of all adsorption processes, the incorporation of labour and material intensive coolant pipes into an adsorbent bed (a component of the considerable infrastructure cost for carbon capture) is necessary to maintain isothermal adsorption conditions. The rate of heat transfer from a sorbent bed to the coolant pipes, which contain surface temperature water at ~25 °C, is primarily dependent on the heat transfer coefficient of the sorbent, the total contact area between the sorbent and the coolant pipes, and the temperature differential between the sorbent and the coolant[39]. The physical size of adsorption units is dictated, to a great extent, by the need to provide sufficient contact area between the coolant and sorbent for effective heat removal. For processes that are limited by heat transfer rather than mass transfer, which is likely for many CO₂ capture processes using solid adsorbents, the use of high temperatures will maximize the temperature differential between the coolant and the sorbent, substantially reducing the overall bed size by reducing the size of the necessary contact area. By increasing the coolant–sorbent temperature differential from about 15 °C to nearly 75 °C, adsorption bed size could potentially be reduced fivefold. In turn, smaller adsorbent beds would reduce the pressure drop across the adsorbent, reduce the size and cost of the required capital equipment, and allow as little as one-fifth as much adsorbent to be used. By decreasing these other system costs, new classes of adsorbents have the ability to reduce the cost of carbon capture substantially beyond simply decreasing the sorbent regeneration energy.

## A functional model for Rubisco

The reactivity trends of the M₂(dobpdc) series may help to clarify the evolutionary conservation of Mg²⁺ within the active site of most photosynthetic enzymes. Biological fixation of atmospheric CO₂ is effected primarily by the ribulose-1,5-bisphosphate carboxylase/oxygenase (Rubisco) enzyme. Striking structural similarities exist between mmen-Mg₂(dobpdc) and the enzymatic pocket of Rubisco, which in its active form also contains an octahedral Mg²⁺ ion ligated by five oxygen donor ligands and a reactive aliphatic amine ligand that adsorbs gas-phase CO₂ to form an O-bound carbamate ligand (Extended Data Fig. 1f)[40,41]. Although other divalent metal ions can be incorporated into either structure, in each case the presence of Mg²⁺ greatly enhances the reactivity for CO₂ fixation at very low CO₂ concentrations[42]. Although further study is necessary, the trends that we observed suggest that the inclusion of Mg²⁺ within the active site of Rubisco may be necessary to endow the lysine residue that forms the enzymatically competent carbamate-ligated metal with sufficient reactivity at low partial pressures of CO₂.

1. International Energy Agency. *CO₂ Emissions from Fuel Combustion: Highlights* <http://www.iea.org/publications/freepublications/publication/CO2EmissionsFromFuelCombustionHighlights2013.pdf> (IEA, 2013).
2. IPCC. in *Climate Change 2013: The Physical Science Basis. Contribution of Working Group I to the Fifth Assessment Report of the Intergovernmental Panel on Climate Change* (eds Stocker, T. F. *et al.*) 11–14 (Cambridge Univ. Press, 2013).

3. Orr, J. C. et al. Anthropogenic ocean acidification over the twenty-first century and its impact on calcifying organisms. *Nature* **437**, 681–686 (2005).
4. Haszeldine, R. S. Carbon capture and storage: how green can black be? *Science* **325**, 1647–1652 (2009).
5. Boot-Handford, M. E. et al. Carbon capture and storage update. *Energy Environ. Sci.* **7**, 130–189 (2014).
6. Choi, S., Drese, J. H. & Jones, C. W. Adsorbent materials for carbon dioxide capture from large anthropogenic point sources. *ChemSusChem* **2**, 796–854 (2009).
7. Lin, L. C. et al. In silico screening of carbon-capture materials. *Nature Mater.* **11**, 633–641 (2012).
8. Sumida, K. et al. Carbon dioxide capture in metal-organic frameworks. *Chem. Rev.* **112**, 724–781 (2012).
9. Zhou, H.-C., Long, J. R. & Yaghi, O. M. Introduction to metal-organic frameworks. *Chem. Rev.* **112**, 673–674 (2012).
10. Furukawa, H., Cordova, K. E., O'Keeffe, M. & Yaghi, O. M. The chemistry and applications of metal-organic frameworks. *Science* **341**, 123044 (2013).
11. Demessence, A., D'Alessandro, D. M., Foo, M. L. & Long, J. R. Strong $CO_2$ binding in a water stable triazolate-bridged metal-organic framework functionalized with ethylenediamine. *J. Am. Chem. Soc.* **131**, 8784–8786 (2009).
12. McDonald, T. M., D'Alessandro, D. M., Krishna, R. & Long, J. R. Enhanced carbon dioxide capture upon incorporation of N,N'-dimethylethylenediamine in the metal-organic framework CuBTTri. *Chem. Sci.* **2**, 2022–2028 (2011).
13. McDonald, T. M. et al. Capture of carbon dioxide from air and flue gas in the alkylamine-appended metal-organic framework mmen-$Mg_2$(dobpdc). *J. Am. Chem. Soc.* **134**, 7056–7065 (2012).
14. Hong, C. S. et al. Diamine-functionalized metal-organic framework: exceptionally high $CO_2$ capacities from ambient air and flue gas, ultrafast $CO_2$ uptake rate, and adsorption mechanism. *Energy Environ. Sci.* **7**, 744–751 (2014).
15. Rosi, N. L. et al. Rod packings and metal-organic frameworks constructed from rod-shaped secondary building units. *J. Am. Chem. Soc.* **127**, 1504–1518 (2005).
16. Dietzel, P. D. C., Panella, B., Hirscher, M., Blom, R. & Fjellvåg, H. Hydrogen adsorption in a nickel based coordination polymer with open metal sites in the cylindrical cavities of the desolvated framework. *Chem. Commun.* 959–961 (2006).
17. Caskey, S. R., Wong-Foy, A. G. & Matzger, A. J. Dramatic tuning of carbon dioxide uptake via metal substitution in a coordination polymer with cylindrical pores. *J. Am. Chem. Soc.* **130**, 10870–10871 (2008).
18. Mason, J. A. et al. Evaluating metal-organic frameworks for post-combustion carbon dioxide capture via temperature swing adsorption. *Energy Environ. Sci* **4**, 3030–3040 (2011).
19. Coelho, A. A. Whole-profile structure solution from powder diffraction powder using simulated annealing. *J. Appl. Crystallogr.* **33**, 899–908 (2000).
20. Planas, N. et al. The mechanism of carbon dioxide adsorption in an alkylamine-functionalized metal-organic framework. *J. Am. Chem. Soc.* **135**, 7402–7405 (2013).
21. Tiritiris, I. & Kantlehner, W. Orthoamide und Iminiumsalze, LXX [1]. Zur Fixierung von Kohlendioxid mit organischen Basen (Teil 1): Reaktionen von Diaminen mit Kohlendioxid. *Z. Naturforsch.* **66b**, 164–176 (2011).
22. Drisdell, W. S. et al. Probing adsorption interactions in metal-organic frameworks using X-ray spectroscopy. *J. Am. Chem. Soc.* **135**, 18183–18190 (2013).
23. Weiss, J. N. The Hill equation revisited: uses and misuses. *FASEB J.* **11**, 835–841 (1997).
24. Irving, H. & Williams, R. J. P. The stability of transition-metal complexes. *J. Chem. Soc.* **637**, 3192–3210 (1953).
25. Perdew, J. P., Burke, K. & Ernzerhof, M. Generalized gradient approximation made simple. *Phys. Rev. Lett.* **77**, 3865–3868 (1996).
26. Walton, K. S. et al. Understanding inflections and steps in carbon dioxide adsorption isotherms in metal-organic frameworks. *J. Am. Chem. Soc.* **130**, 406–407 (2008).
27. Horike, S., Shimomura, S. & Kitagawa, S. Soft porous crystals. *Nature Chem.* **1**, 695–704 (2009).
28. Serre, C. et al. Very large breathing effect in the first nanoporous chromium(lll)-based solids: MIL-53 or $Cr^{III}(OH)\cdot\{O_2C-C_6H_4-CO_2\}\cdot\{HO_2C-C_6H_4-CO_2H\}_x\cdot\{H_2O\}_y$. *J. Am. Chem. Soc.* **124**, 13519–13526 (2002).
29. Henke, S. et al. Multiple phase-transitions upon selective $CO_2$ adsorption in an alkyl ether functionalized metal-organic framework—an in situ X-ray diffraction study. *CrystEngComm* **13**, 6399–6404 (2011).
30. Seo, J., Matsuda, R., Sakamoto, H., Bonneau, C. & Kitagawa, S. A pillared-layer coordination polymer with a rotable pillar acting as a molecular gate for guest molecules. *J. Am. Chem. Soc.* **131**, 12792–12800 (2009).
31. Thomy, A. & Duval, X. Stepwise isotherms and phase transitions in physisorbed films. *Surf. Sci.* **299–300**, 415–425 (1994).
32. Jessop, P. G., Mercer, S. M. & Heldebrant, D. J. $CO_2$-triggered switchable solvents, surfactants, and other materials. *Energy Environ. Sci.* **5**, 7240–7253 (2012).
33. Liebenthal, U. et al. Overall process analysis and optimisation for $CO_2$ capture from coal fired power plants based on phase change solvents forming two liquid phases. *Energy Procedia* **37**, 1844–1854 (2013).
34. Ma'mun, S. & Kim, I. Selection and characterization of phase-change solvent for carbon dioxide capture: precipitating system. *Energy Procedia* **37**, 331–339 (2013).
35. Choi, S., Watanabe, T., Bae, T.-H., Sholl, D. S. & Jones, C. W. Modification of the Mg/DOBDC MOF with amines to enhance $CO_2$ adsorption from ultradilute gases. *J. Phys. Chem. Lett.* **3**, 1136–1141 (2012).
36. Rochelle, G. et al. Aqueous piperazine as the new standard for $CO_2$ capture technology. *Chem. Eng. J.* **171**, 725–733 (2011).
37. Sayari, A. & Belmabkhout, Y. Stabilization of amine-containing $CO_2$ adsorbents: dramatic effect of water vapor. *J. Am. Chem. Soc.* **132**, 6312–6314 (2010).
38. Nugent, P. et al. Porous materials with optimal adsorption thermodynamics and kinetics for $CO_2$ separation. *Nature* **495**, 80–84 (2013).
39. van Lare, C. E. J. Mass Transfer in Gas Fluidized Beds: Scaling, Modeling, and Particle Size Influence 141–142. PhD thesis, Tech. Univ. Eindhoven (1991) <http://alexandria.tue.nl/repository/books/348157.pdf>.
40. Lorimer, G. The carboxylation and oxygenation of ribulose 1,5–bisphosphate: the primary events in photosynthesis and photorespiration. *Annu. Rev. Plant Physiol.* **32**, 349–382 (1981).
41. Taylor, T. C. & Andersson, I. Structural transitions during activation and ligand binding in hexadecameric Rubisco inferred from the crystal structure of activated unliganded spinach enzyme. *Nature Struct. Biol.* **3**, 95–101 (1996).
42. Assche, F. & Clijsters, H. Effects of metals on enzyme activity in plants. *Plant Cell Environ.* **13**, 195–206 (1990).

## METHODS

**General synthesis and characterization methods.** All reagents and solvents were obtained from commercial sources at reagent-grade purity or higher. The compound $H_4(dobpdc)$ was synthesized as reported previously[13]. No statistical methods were used to predetermine sample size.

Laboratory powder X-ray diffraction patterns were collected on a Bruker AXS D8 Advance diffractometer equipped with Cu Kα radiation ($\lambda = 1.5418$ Å), a Göbel mirror, a Lynxeye linear position-sensitive detector, and mounting the following optics: fixed divergence slit (0.6 mm), receiving slit (3 mm) and secondary-beam Soller slits (2.5°). The generator was set at 40 kV and 40 mA. Owing to the oxygen sensitivity of $Fe_2(dobpdc)$ and mmen-$Fe_2(dobpdc)$, X-ray diffraction patterns were collected in sealed glass capillaries placed on the powder stage. Thermogravimetric analysis was carried out at a ramp rate of $2\,°C\,min^{-1}$ in a nitrogen flow with a TA Instruments Q5000. Elemental analyses for C, H and N were performed at the Microanalytical Laboratory of the University of California, Berkeley.

**Synthesis of $Mg_2(dobpdc)$.** To a 20 ml glass scintillation vial, $H_4dobpdc$ (27.4 mg, 0.10 mmol), $Mg(NO_3)_2 \cdot 6H_2O$ (64.0 mg, 0.25 mmol) and 10 ml of mixed solvent (55:45 methanol/dimethylformamide (DMF)) were added. The vial was sealed with a polytetrafluoroethylene (PTFE)-lined cap and placed in a well plate 2 cm deep on a 393 K hot plate. After 12 h a white powder formed on the bottom and walls of the vial. The reaction mixture was then decanted and the remaining powder was soaked three times in DMF and then three times in methanol. The solid was then collected by filtration and fully desolvated by heating under dynamic vacuum (<10 µbar) at 523 K for 24 h to afford 23.3 mg (0.073 mmol), 73% of $Mg_2(dobpdc)$. Combustion elemental analysis calculated (Anal. Calcd for $C_{14}H_6O_6Mg_2$: C, 52.74; H, 1.90. Found: C, 52.47; H, 1.64.

**Synthesis of $Mn_2(dobpdc)$.** To a 20 ml glass scintillation vial, $H_4dobpdc$ (27.4 mg, 0.10 mmol), $MnCl_2 \cdot 4H_2O$ (49.5 mg, 0.25 mmol), and 10 ml of mixed solvent (1:1 ethanol/DMF) were added. The vial was sealed with a PTFE-lined cap and placed in a well plate 2 cm deep on a 393 K hot plate. After 12 h a yellow powder formed on the bottom and walls of the vial. The reaction mixture was then decanted and the remaining powder was soaked three times in DMF and then three times in methanol. The solid was then collected by filtration and fully desolvated by heating under dynamic vacuum (<10 µbar) at 523 K for 24 h to afford 33.8 mg (0.0889 mmol), 89% of $Mn_2(dobpdc)$. Anal. Calcd for $C_{14}H_6O_6Mn_2$: C, 44.24; H, 1.59. Found: C, 44.32; H, 1.23.

**Synthesis of $Fe_2(dobpdc)$.** Anhydrous $FeCl_2$ (2.85 g, 22.4 mmol), $H_4dobpdc$ (1.85 g, 6.75 mmol), anhydrous DMF (400 ml) and anhydrous methanol (50 ml) were added to a 500 ml Shlenck flask under an argon atmosphere. The reaction mixture was heated to 393 K and stirred for 24 h to afford a dark yellow-green precipitate. The solvent was then removed by cannula transfer and replaced with fresh anhydrous DMF. The reaction mixture was soaked three times in DMF and then three times in methanol. The solid was then fully desolvated by heating under dynamic vacuum (<10 µbar) at 523 K for 24 h to afford 2.395 g (6.28 mmol), 93% of $Fe_2(dobpdc)$. Anal. Calcd for $C_{14}H_6O_6Fe_2$: C, 44.03; H, 1.58. Found: C, 43.72; H, 1.48.

**Synthesis of $Co_2(dobpdc)$.** To a 20 ml glass scintillation vial, $H_4dobpdc$ (41.1 mg, 0.15 mmol), $Co(NO_3)_2 \cdot 6H_2O$ (109 mg, 0.375 mmol) and 15 ml of mixed solvent (1:1:1 water/DMF/ethanol) were added. The vial was sealed with a PTFE-lined cap and placed in a well plate 2 cm deep on a 393 K hot plate. After 36 h a pink powder formed on the bottom of the vial. The reaction mixture was then decanted and the remaining powder was soaked three times in DMF and then three times in methanol. The solid was then collected by filtration and fully desolvated by heating under dynamic vacuum (<10 µbar) at 523 K for 24 h to afford 54.1 mg (0.139 mmol), 93% of $Co_2(dobpdc)$. Anal. Calcd for $C_{14}H_6O_6Co_2$: C, 43.33; H, 1.56. Found: C, 42.92; H, 1.38.

**Synthesis of $Zn_2(dobpdc)$.** To a 20 ml glass scintillation vial, $H_4dobpdc$ (27.4 mg, 0.10 mmol), $ZnBr_2 \cdot 2H_2O$ (83.5 mg, 0.32 mmol) and 10 ml of mixed solvent (1:1 ethanol/DMF) were added. The vial was sealed with a PTFE-lined cap and placed in a well plate 2 cm deep on a 393 K hot plate. After 12 h a pale yellow powder formed on the bottom and walls of the vial. The reaction mixture was then decanted and the remaining powder was soaked three times in DMF and then three times in methanol. The solid was then collected by filtration and fully desolvated by heating under dynamic vacuum (<10 µbar) at 523 K for 24 h to afford 21.4 mg (0.0534 mmol), 53% of $Zn_2(dobpdc)$. Anal. Calcd for $C_{14}H_6O_6Zn_2$: C, 41.94; H, 1.51. Found: C, 41.26; H, 1.57.

**Synthesis of $Ni_2(dobpdc)$.** To a 20 ml glass scintillation vial, $H_4dobpdc$ (41.1 mg, 0.150 mmol), $Ni(NO_3)_2 \cdot 6H_2O$ (109 mg, 0.375 mmol) and 15 ml of mixed solvent (1:1:1 water/DMF/ethanol) were added. The vial was sealed with a PTFE-lined cap and placed in a well plate 2 cm deep on a 393 K hot plate. After 36 h, a green powder formed on the bottom of the vial. The reaction mixture was then decanted and the remaining powder was soaked three times in in DMF and then three times in methanol. The solid was then collected by filtration and fully desolvated by heating under

dynamic vacuum (<10 µbar) at 523 K for 24 h to afford 39.3 mg (0.101 mmol), 68% of $Ni_2(dobpdc)$. Anal. Calcd for $C_{14}H_6O_6Ni_2$: C, 43.39; H, 1.56. Found: C, 43.09; H, 1.24.

**General synthesis of mmen-$M_2(dobpdc)$.** In a plastic glovebag with positive $N_2$ pressure, 10 ml of 10% mmen solution in hexanes was added to ∼100 mg of activated $M_2(dobpdc)$ in a glass Micromeritics adsorption tube. The tube was sealed with a rubber septum and left to sit undisturbed for 4 h in the glovebag. In the glovebag, the sample was collected by vacuum filtration and rinsed with five 10 ml portions of dry hexanes. The hexanes-solvated sample was desolvated under dynamic vacuum (<10 µbar) at 348 K (for Zn) or 373 K (for Mg, Mn, Fe, Co and Ni) for 4 h.

**Elemental analysis of mmen-$M_2(dobpdc)$ series.** Mg: Anal. Calcd for $C_{22}H_{30}N_4O_6Mg_2$: C, 53.37; H, 6.11; N, 11.32. Found: C, 52.39; H, 5.52; N, 10.36. Mn: $C_{22}H_{30}N_4O_6Mn_2$: C, 47.47; H, 5.43; N, 10.07. Found: C, 47.26; H, 5.20; N, 10.24. Fe: Anal. Calcd for $C_{22}H_{30}N_4O_6Fe_2$: C, 47.34; H, 5.42; N, 10.04. Found: C, 47.; H, 4.95; N, 9.71. Co: Anal. Calcd for $C_{22}H_{30}N_4O_6Co_2$: C, 46.82; H, 5.36; N, 9.93. Found: C, 46.27; H, 4.94; N, 9.61. Zn: Anal. Calcd for $C_{22}H_{26}N_4O_6Zn_2$: C, 45.78; H, 5.24; N, 9.71. Found: C, 45.46; H, 4.75; N, 9.78. Ni: Anal. Calcd for $C_{22}H_{30}N_4O_6Ni_2$: C, 46.86; H, 5.36; N, 9.94. Found: C, 46.68; H, 5.33; N, 10.28.

**Low-pressure gas adsorption measurements.** For all low-pressure (0–1.1 bar) gas adsorption measurements, 60–130 mg of adsorbent was transferred to a pre-weighed glass sample tube under an atmosphere of nitrogen gas and capped with a Transeal. Samples were then transferred manually to a Micromeritics ASAP 2020 gas adsorption analyser and heated to the activation temperatures previously specified, under vacuum. The sample was considered activated when the outgas rate was less than $2\,\mu bar\,min^{-1}$. The evacuated tube containing the activated sample was then transferred to a balance and weighed to determine the mass of the desolvated sample. The tube was then placed manually on the analysis port of the aforementioned instrument, where the outgas rate was once again confirmed to be less than $2\,\mu bar\,min^{-1}$. Isothermal conditions were maintained at 77 K with liquid $N_2$, at 25, 40, 50 and 75 °C with a Julabo F32 water circulator, and at 100 °C with a heated sand bath controlled by a programmable temperature controller.

**High-pressure gas adsorption measurements.** The high-pressure $CO_2$ adsorption isotherm for mmen-$Ni_2(dobpdc)$ was measured on a HPVA-II-100 from Particulate Systems, a Micromeritics company. Here, 0.27 g of activated mmen-$Ni_2(dobpdc)$ was loaded into a tared 2 ml stainless steel sample holder inside a glovebox under a $N_2$ atmosphere. Before the sample holder was connected to the variable compression ratio fittings of the high-pressure assembly inside the glovebox, the sample holder was weighed to determine the sample mass.

Before mmen-$Ni_2(dobpdc)$ was measured, 25 °C $CO_2$ background measurements were performed on a sample holder containing nonporous glass beads that occupied a similar volume as a typical sample. A small negative background was observed at higher pressures, which may have been due to errors in volume calibrations, temperature calibrations and/or the equation of state used to perform the nonideality corrections. Nevertheless, the background $CO_2$ adsorption was consistent across several measurements and was well described by fitting to a polynomial equation. This polynomial was then used to perform a background subtraction on the raw high-pressure $CO_2$ data for mmen-$Ni_2(dobpdc)$.

***In situ* infrared spectroscopy.** A powdered sample of mmen-$Mg_2(dobpdc)$ (∼15 mg) was pelletized, shaped in a self-supported wafer and placed inside a commercial Fourier-transform infrared reactor cell (2000-A multimode; AABSPEC), which allowed infrared spectra to be recorded under flow conditions at a wide range of temperatures. Before $CO_2$ was flowed across the sample, the sample was first activated at 150 °C for 15 min while flowing $30\,ml\,min^{-1}$ of pure nitrogen (heating ramp rate of $1\,°C\,min^{-1}$). Next, the gas flow was switched to 5% $CO_2$ in $N_2$ at a flow rate of $30\,ml\,min^{-1}$, and the system was cooled from 150 °C to 30 °C at a rate of $1\,°C\,min^{-1}$. Before cooling, the sample was conditioned for 15 min at 150 °C with the 5% $CO_2$ in $N_2$ gas mixture. After cooling to 30 °C, the sample was heated again to 150 °C at a rate of $5\,°C\,min^{-1}$ under $N_2$, to check the reversibility of the process. Spectra were collected every 5 °C with a resolution of $2\,cm^{-1}$ (number of scans equal to 32) on a Perkin-Elmer System 2000 infrared spectrophotometer equipped with a HgCdTe detector. For Extended Data Fig. 2c, curve-fitting analysis was performed with the Levenberg–Maquardt method by using the OPUS software (Bruker Optik); 100% Gauss functions were used.

For Extended Data Fig. 2b, the attenuated total reflectance (ATR) accessory of a Perkin-Elmer Spectrum 400 was enclosed within a plastic glovebag filled with positive gas pressure. Spectra of activated adsorbent were collected first under a $N_2$ atmosphere. After 32 scans at a resolution of $4\,cm^{-1}$, the glovebag was allowed to fill with $CO_2$ for 5 min and infrared spectra of the sample were collected again under an atmosphere of $CO_2$. For Extended Data Fig. 2e, a gas mixture of 20 mbar $H_2O$, 150 mbar $CO_2$ and 600 mbar $N_2$ was dosed onto an activated sample of mmen-$Mg_2(dobpdc)$ and was left to equilibrate for 6 h before being placed on the ATR stage of a glovebag-encased Spectrum 400 instrument.

**Solid-state NMR spectroscopy.** Solid-state NMR experiments were performed on a 7.05 T magnet with a Tecmag Discovery spectrometer, using a Doty 5 mm triple-resonance magic angle spinning probe. The frequency of $^{15}N$ was 30.4 MHz. $^{15}N$ chemical shifts were referenced to $^{15}N$-labelled glycine at 33 p.p.m. relative to liquid ammonia. The experiments were performed at ambient temperature. Magic angle spinning was used to collect high-resolution NMR spectra with a spinning rate ranging from 5 to 6 kHz. The 90° pulses for $^1H$, $^{13}C$ and $^{15}N$ were 3.8, 4.7 and 7 μs, respectively. Ramped cross-polarization with variable contact times from 1 to 10 ms was used to generate $^{15}N$ signals. Recycle delays were set to be fivefold longer than the $T_1$ of protons. Two-pulse phase-modulated $^1H$ decoupling of 100 kHz was applied during $^{15}N$ signal acquisition.

**Isobaric $CO_2$ adsorption methods.** Isobaric gravimetric adsorption experiments were collected using a TA Instruments Q5000 analyser using premixed gas cylinders (Praxair). A flow rate of 25 ml min$^{-1}$ was employed for all gases. Before each experiment, the samples (~5 mg) were desolvated by heating under $N_2$ for 1 h. To simulate temperature swing adsorption processes accurately, samples were activated and reactivated with only 100% $CO_2$. Sample masses were normalized to 0% under a 100% $CO_2$ atmosphere ~10 s before the onset of each cooling cycle. Thus, the base mass corresponds to the weight of the metal-organic framework and any $CO_2$ adsorbed under the activation conditions: 150 °C for mmen-Mg$_2$(dobpdc) and 120 °C for mmen-Mn$_2$(dobpdc). Masses were uncorrected for buoyancy effects.

For Fig. 6a, b, ramp rates of 1 °C min$^{-1}$ were used; samples were reactivated at the appropriate regeneration temperature under 100% $CO_2$ for 15 min between gases. Switching from 100% $CO_2$ to a lower concentration of $CO_2$ occurred at the onset of cooling, ensuring that the lower-concentration gas would not simulate a purge gas for regeneration.

For Fig. 6c, d, ramp rates of 10 °C min$^{-1}$ were used. Samples were heated between the adsorption and regeneration conditions under 100% $CO_2$; the regeneration time was 5 min. Samples were cooled under low-concentration $CO_2$; the adsorption time was 5 min. Total cycle time was ~20 min.

**High-resolution powder X-ray diffraction.** Samples of fully activated mmen-Mn$_2$(dobpdc) microcrystalline powders (~10 mg) were loaded into 1.0 mm boron-rich glass capillaries inside a glovebox under an $N_2$ atmosphere. The capillaries were attached to a gas cell, which was connected to the analysis port of a Micromeritics ASAP-2020 gas adsorption instrument. The capillaries were fully evacuated at room temperature for 30 min, dosed with 5 mbar of He [mmen-Mn$_2$(dobpdc)], 5 mbar of $CO_2$ (100K-$CO_2$-mmen-Mn$_2$(dobpdc)) or 100 mbar of $CO_2$ (295K-$CO_2$-mmen-Mn$_2$(dobpdc)) and then equilibrated at room temperature for 15 min, 8 h or 4 h, respectively. After equilibration, the capillaries were flame-sealed and placed inside a Kapton tube that was sealed on both ends with epoxy.

High-resolution synchrotron X-ray powder diffraction data were subsequently collected at beamline 11-BM at the Advanced Photon Source (APS), Argonne National Laboratory, with an average wavelength of ~0.4137 Å. Diffraction patterns were collected at 100 K, 100 K and 295 K for mmen-Mn$_2$(dobpdc), 100K-$CO_2$-mmen-Mn$_2$(dobpdc) and 295K-$CO_2$-mmen-Mn$_2$(dobpdc), respectively. Discrete detectors covering an angular range from −6 to 16° 2θ were scanned over a 34° 2θ range, with data points collected every 0.001° 2θ and a scan speed of 0.01° s$^{-1}$. Owing to the large number of collected data points, all diffraction patterns were rebinned to a step size of 0.005° 2θ before structure solution and Rietveld refinement. Additionally, all diffraction patterns showed a high-intensity peak at ~1.25° that was ~500% more intense than any other diffraction peak. Because this high d-spacing peak does not contribute important structural information and was heavily biasing all structure solution attempts, all data analysis was performed with a minimum 2θ of 2°.

A standard peak search, followed by indexing through the Single Value Decomposition approach[43], as implemented in TOPAS-Academic[44], allowed the determination of approximate unit-cell parameters. Tentatively, the space groups for both mmen-Mn$_2$(dobpdc) and $CO_2$-mmen-Mn$_2$(dobpdc) were assigned as $P3_221$ because the framework was expected to be isostructural to Zn$_2$(dobpdc), which was previously characterized by single crystal X-ray diffraction[13]. Precise unit-cell dimensions were determined by structureless Le Bail refinements (Supplementary Table 1). Here, the background was modelled by a polynomial function of the Chebyshev type, and anisotropic peak broadening was described using parameters appropriate for a hexagonal crystal system[45]. Successful structure solution and Rietveld refinement confirmed that $P3_221$ was indeed the correct space group for all compounds.

**Breakthrough adsorption measurements.** Into a glass U-tube with an interior diameter of 4 mm, 203 mg of activated mmen-Mg$_2$(dobpdc) powder was added. The column was placed inside a furnace with a programmable temperature controller. Gas flow rates of 10 ml min$^{-1}$ were used. Column effluent was analysed using a Hy-Energy/Setaram RGAPro-2500 with continuous sampling capability. Argon (99.999%; Praxair) was used as a purge gas for sample activation at 100 °C for 30 min. For measurements at 25 °C, ~1.5% $H_2O$ was added to the gas stream by bubbling a premixed gas cylinder of 15% $CO_2$, 4% $O_2$ and balance $N_2$ (Praxair) through a glass bubbler containing distilled water.

**NEXAFS measurements.** *In situ* NEXAFS measurements were performed with a gas cell instrument previously described in detail elsewhere[22,46]. Transmission–absorption samples were prepared by suspending and sonicating ~10 mg of mmen-Mg$_2$(dobpdc) powder in ~1 ml of hexanes, and drop casting onto SiC membranes (300 nm thickness). The metal-organic framework-coated membranes were then loaded into a glass evacuation chamber that was slowly evacuated to 50 mTorr. The chamber was then heated to 100 °C for 4 h to remove all guest species from the pores. After heating, the chamber was cooled to ambient temperature and refilled with dry nitrogen gas. Samples were transferred from the evacuation chamber to the gas cell in a dry nitrogen glovebox to prevent exposure to any unwanted species. N K-edge spectra of mmen-Mg$_2$(dobpdc) were collected at beamline 6.3.2 ($10^{11}$ photons s$^{-1}$) at the Advanced Light Source at Lawrence Berkeley National Laboratory, under vacuum and increasing pressures of $CO_2$ gas. The experimental procedure was the same as in earlier studies. The full pressure series of N K-edge spectra are shown in Extended Data Fig. 3.

**AIMD simulations.** The equilibrium structure of mmen-Mg$_2$(dobpdc) is obtained by performing constant-pressure (NPT) *ab initio* molecular dynamics simulations at room temperature. The system is equilibrated using a Parrinello–Rahman barostat and a Langevin thermostat with a time step of 0.5 fs (refs 47, 48). A plane-wave basis set that is truncated at 400 eV is used to represent the electronic wavefunctions within the projector-augmented wave (PAW) approximation[49,50], as realized in the Vienna *Ab initio* Simulation Package (VASP)[51,52]. vdW-DF2 functional is used to approximate the long-range dispersion forces[53], which is potentially important to capture the weak intermolecular interactions between the metal-organic framework and the absorbed molecules. Here, the vdW-DF2 correlation is computed with the use of a $1 \times 1 \times 3$ k-point grid to ensure that the electron density is converged for a 22 Å × 21 Å × 7 Å supercell. On equilibration, eight time-separated (that is, uncorrelated) snapshots are taken from the molecular dynamics trajectory to establish an average spectrum from NEXAFS simulations.

**XAS simulations.** DFT calculations used for X-ray absorption spectroscopy (XAS) simulations employ the PBE GGA functional[25]. Plane-wave pseudopotential calculations using ultrasoft pseudopotentials[54] and a kinetic energy cutoff for electronic wavefunctions (density) of 25 (200) Rydberg (Ry) were performed using the PWSCF code within the Quantum-ESPRESSO package[55]. The core-excited Kohn–Sham eigenspectrum was generated using the eXcited electron and Core Hole (XCH) approach. On the basis of a numerically converged self-consistent charge density, we generated the unoccupied states for our XAS calculations non-self-consistently, sufficiently sampling the first Brillouin zone with a $2 \times 2 \times 2$ uniform k-point grid, employing an efficient implementation of the Shirley interpolation scheme[56] generalized to handle ultrasoft pseudopotentials[57]. Matrix elements were evaluated within the PAW frozen-core approximation[58]. Core-excited ultrasoft pseudopotentials and corresponding atomic orbitals were generated with the Vanderbilt code[54]. Each computed transition was convoluted with a 0.2 eV Gaussian function to produce continuous spectra.

**Periodic DFT calculations.** Periodic DFT calculations in this work were performed with the VASP 5.3.3 package[51,59]. The energetics of $CO_2$ capture by the alkylamine moieties chemisorbed in the channels of M$_2$(dobpdc) (M = Mg, Mn, Fe, Co, Ni, Zn) were computed with the PBE and M06L functionals[25,60]. The electron–ion interactions in these calculations were described with the PAW method[49] with an energy cutoff of 550 eV. Atomic positions and lattice parameters were optimized until the forces on all atoms were smaller than 0.02 eV Å$^{-1}$ at the Γ-point. On-site Hubbard $U$ corrections were employed for metal d electrons for M$_2$(dobpdc) (M = Mn, Fe, Co, Ni)[61]. The $U$ values are determined to reproduce oxidation energies in the respective metal oxides[62].

**Modelled adsorption isotherms.** To study the differences in adsorption behaviour between the pair and chain models, we used a lattice model to predict the adsorption isotherms. The lattice models are illustrated in Extended Data Fig. 5. The energy at each lattice point is determined by the state of the lattice point and the state of the surrounding lattice points. For both the pair and the chain model the interaction energies, yellow and red, respectively, are taken directly from the DFT calculations. The end of a chain (shown in blue) is 80% of the chain model, whereas a single adsorbed $CO_2$ (shown in green) is 10% of the energy of a chain. Similarly, interactions between two rows (cross-channel) are set to the pair energy (or 75% of a chain). An amine without $CO_2$ was not given an energy contribution. The effect of having different metals was taken into account by varying the energy of the chain in accordance with the DFT energies. To compute the isotherms we performed standard grand-canonical Monte Carlo simulations. To compare the lattice model chemical potential directly with the chemical potential of $CO_2$ we used a shift of the pressure, which was fitted to the steps of the isotherms at the highest and lowest temperatures.

43. Coelho, A. A. Indexing of powder diffraction patterns by iterative use of singular value decomposition. *J. Appl. Crystallogr.* **36,** 86–95 (2003).
44. Coelho, A. A. *TOPAS-Academic, Version 4.1* (Coelho Software, 2007).

45. Stephens, P. W. Phenomenological model of anisotropic peak broadening in power diffraction. *J. Appl. Crystallogr.* **32**, 281–289 (1999).
46. Drisdell, W. S. & Kortright, J. B. Gas cell for *in situ* soft X-ray transmission-absorption spectroscopy of materials. *Rev. Sci. Instrum.* **85**, 074103 (2014).
47. Allen, M. P. & Tildesley, D. J. *Computer Simulation of Liquids* (Clarendon Press, 1987).
48. Parrinello, M. & Rahman, A. Crystal structure and pair potentials: a molecular-dynamics study. *Phys. Rev. Lett.* **45**, 1196–1199 (1980).
49. Blöchl, P. E. Projector augmented-wave method. *Phys. Rev. B* **50**, 17953–17978 (1994).
50. Kresse, G. & Joubert, D. From ultrasoft pseudopotentials to the projector augmented-wave method. *Phys. Rev. B* **59**, 1758–1775 (1999).
51. Kresse, G. & Furthmuller, J. Efficiency of ab-initio total energy calculations for metals and semiconductors using a plane-wave basis set. *Comput. Mater. Sci.* **6**, 15–50 (1996).
52. Kresse, G. & Hafner, J. Ab initio molecular-dynamics for liquid-metals. *Phys. Rev. B* **47**, 558–561 (1993).
53. Lee, K., Murray, E. D., Kong, L., Lundqvist, B. I. & Langreth, D. C. Higher-accuracy van der Waals density functional. *Phys. Rev. B* **82**, 081101 (2010).
54. Vanderbilt, D. Soft self-consistent pseudopotentials in a generalized eigenvalue formalism. *Phys. Rev. B* **41**, 7892–7895 (1990).
55. Giannozzi, P. *et al.* QUANTUM ESPRESSO: a modular and open-source software project for quantum simulations of materials. *J. Phys. Condens. Matter* **21**, 395502 (2009).
56. Shirley, E. L. Optimal basis sets for detailed Brillouin-zone integrations. *Phys. Rev. B* **54**, 16464–16469 (1996).
57. Prendergast, D. & Louie, S. G. Bloch-state-based interpolation: an efficient generalization of the Shirley approach to interpolating electronic structure. *Phys. Rev. B* **80**, 235126 (2009).
58. Taillefumier, M., Cabaret, D., Flank, A.-M. & Mauri, F. X-ray absorption near-edge structure calculations with the pseudopotentials: application to the K edge in diamond and $\alpha$-quartz. *Phys. Rev. B* **66**, 195107 (2002).
59. Kresse, G. & Furthmuller, J. Efficient iterative schemes for ab initio total-energy calculations using a plane-wave basis set. *Phys. Rev. B* **54**, 11169–11186 (1996).
60. Zhao, Y. & Truhlar, D. G. A new local density functional for main-group thermochemistry, transition metal bonding, thermochemical kinetics, and noncovalent interactions. *J. Chem. Phys.* **125**, 194101 (2006).
61. Liechtenstein, A. I., Anisimov, V. I. & Zaanen, J. Density-functional theory and strong interactions: orbital ordering in Mott–Hubbard insulators. *Phys. Rev. B* **52**, R5467–R5470 (1995).
62. Wang, L., Maxisch, T. & Ceder, G. Oxidation energies of transition metal oxides within the GGA+U framework. *Phys. Rev. B* **73**, 195107 (2006).
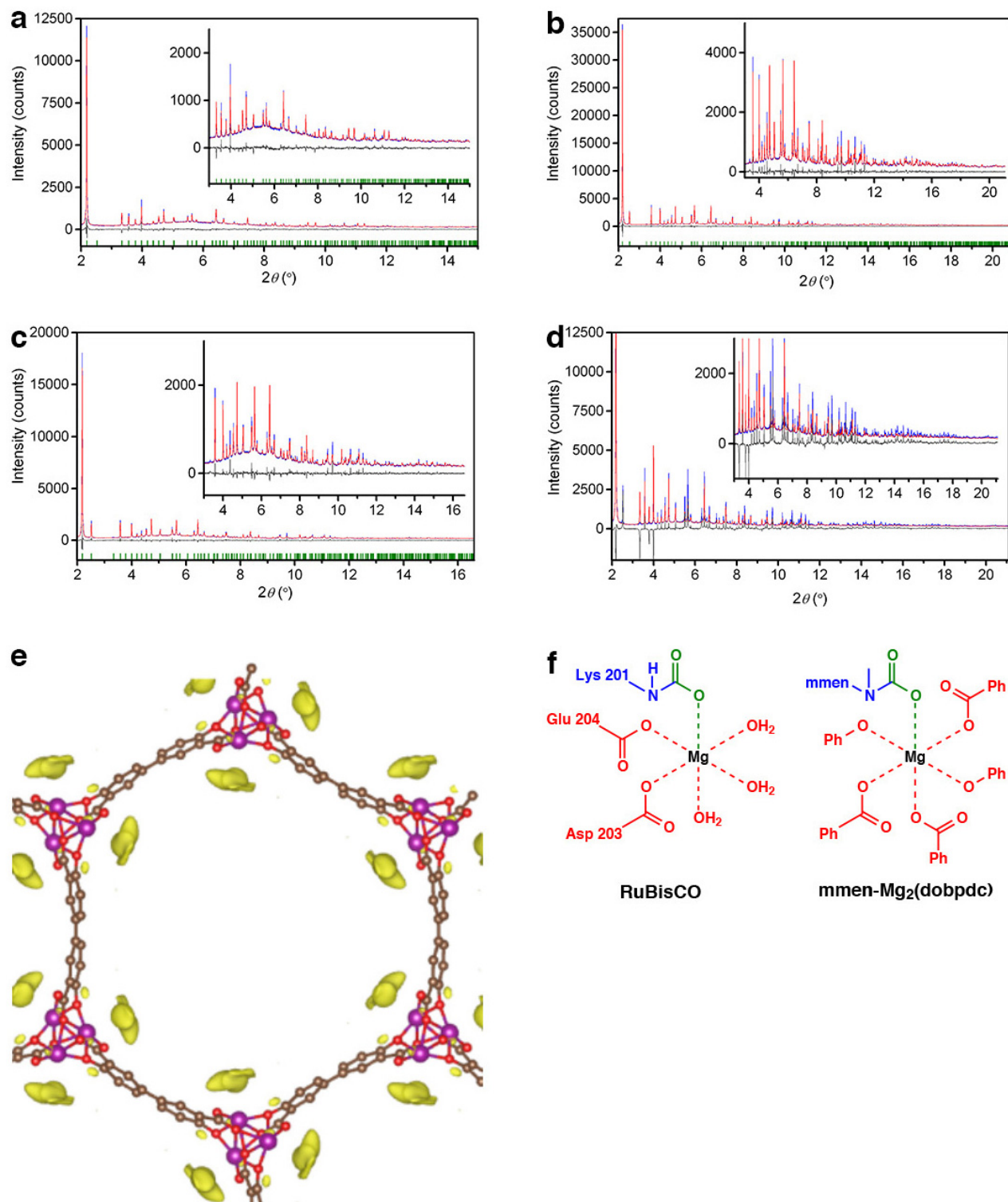
**Extended Data Figure 1 | Powder X-ray diffraction. a–c**, Rietveld refinement of mmen-Mn$_2$(dobpdc) at 100 K (**a**), CO$_2$-mmen-Mn$_2$(dobpdc) at 100 K (**b**) and CO$_2$-mmen-Mn$_2$(dobpdc) at 295 K (**c**). The blue and red lines represent the experimental and calculated diffraction patterns, respectively; the grey line represents the difference between experimental and calculated patterns; the green tick marks represent the calculated Bragg peak positions. **d**, Plot of the diffraction data for CO$_2$-mmen-Mn$_2$(dobpdc) at 100 K (blue), where the calculated pattern (red) is based on the mmen-Mn$_2$(dobpdc) structural model. The grey line represents the difference between the experimental and calculated patterns. Note that the intensity differences indicate a structural transition when CO$_2$ is adsorbed. **e**, Fourier difference map for mmen-Mn$_2$(dobpdc) at 100 K. Purple, brown and red spheres represent Mn, C and O atoms, respectively; yellow blobs represent excess electron density that is not accounted for in the Mn$_2$(dobpdc) structural model and that is due to the mmen bound to each Mn$^{2+}$ site. **f**, The coordination environment around Mg$^{2+}$ in the active form of the Rubisco enzyme is structurally similar to the coordination environment around the metal cations of mmen-Mg$_2$(dobpdc) after adsorption of CO$_2$.
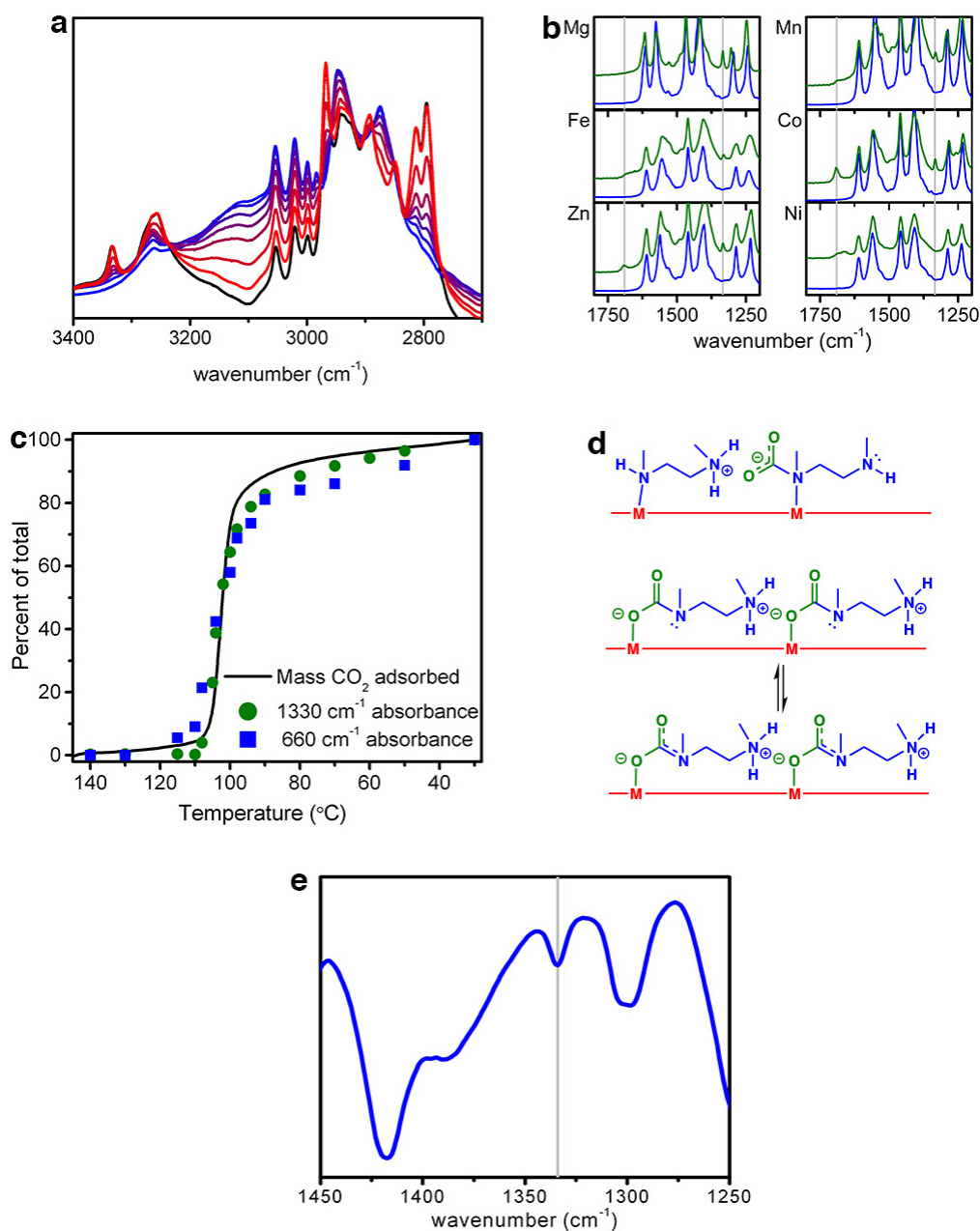
**Extended Data Figure 2 | Infrared spectroscopy. a**, On cooling mmen-Mg₂(dobpdc) from 150 °C (red) to 30 °C (blue) under 5% CO₂, changes to the aliphatic C–H vibrations of mmen are apparent on adsorption of CO₂. Furthermore, ammonium formation from neutral secondary amines is indicated by the appearance of a new, broad feature centred on 3,000 cm⁻¹. **b**, Room temperature, *in situ* infrared spectroscopy measurements of mmen-M₂(dobpdc) (M = Mg, Mn, Fe, Co, Zn, Ni) under N₂ (blue) and CO₂ (green) atmospheres. Grey lines mark diagnostic carbamate bands at 1,690 and 1,334 cm⁻¹. **c**, On cooling under flowing 5% CO₂ in N₂ from 150 to 30 °C, the normalized mass increase of mmen-Mg₂(dobpdc) measured by thermogravimetric analysis (black line) can be compared with the normalized integrated area of the infrared active bands at 1,330 and 660 cm⁻¹. The bands at 1,330 and 660 cm⁻¹ can be assigned to ν(C–N) and [β(OCO) + β(NCO)] modes that are characteristic of the highly ordered ammonium carbamate chains. **d**, In contrast to carbamate that is coordinated to a metal site through a nitrogen atom (top), changes in electron resonance configurations give rise to a feature at 1,334 cm⁻¹ characteristic of CO₂ insertion into the metal–nitrogen bond (bottom). **e**, Infrared spectroscopy clearly indicates that CO₂ adsorption via metal-amine insertion occurs even in the presence of H₂O owing to the presence of the aforementioned band at 1,334 cm⁻¹.
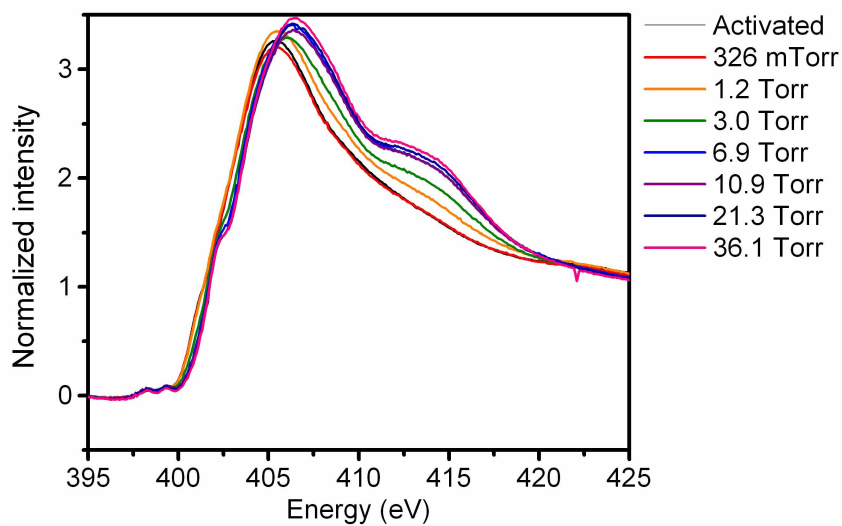
**Extended Data Figure 3 | X-ray absorption spectroscopy.** Experimental N K-edge NEXAFS spectra of mmen-Mg$_2$(dobpdc) in vacuum and under increasing pressures of CO$_2$ gas. The broad feature between 411 and 419 eV, a signature of N–C bond formation, appears before the pre-edge peak at 402.3 eV, which is characteristic of CO$_2$ insertion.
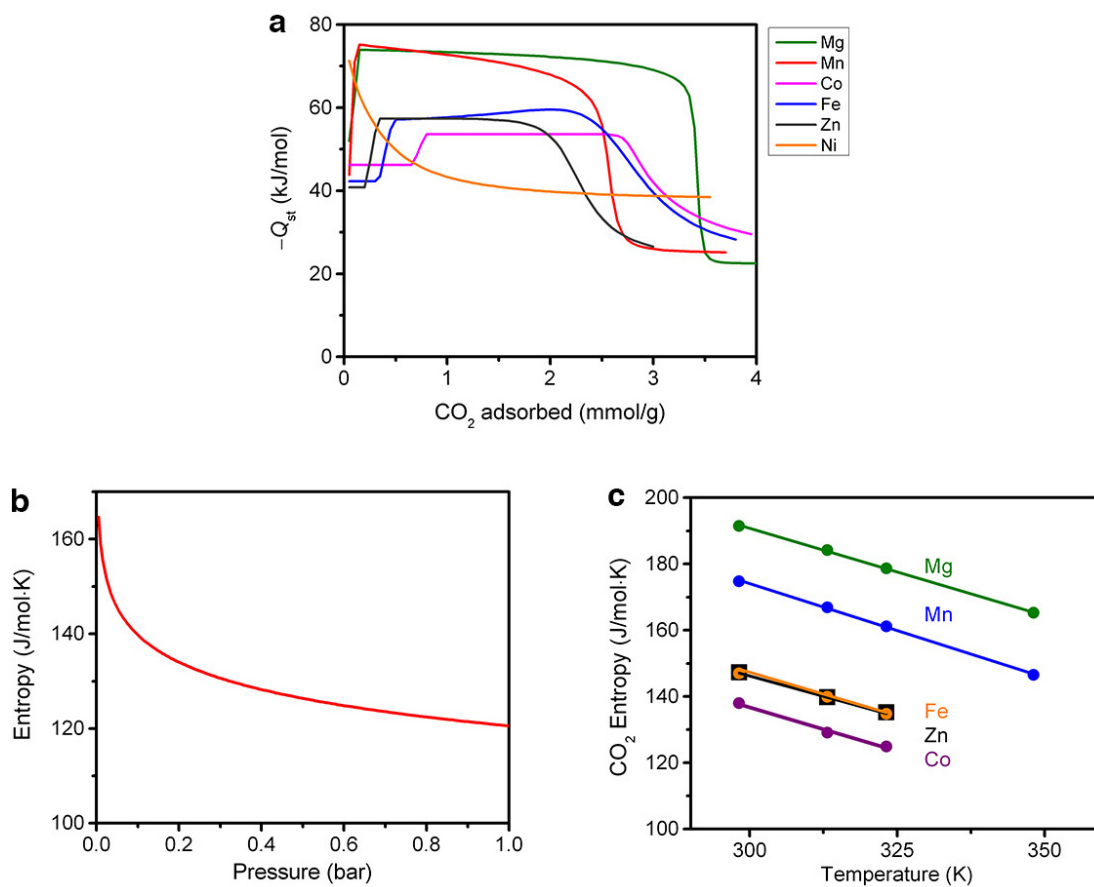
**Extended Data Figure 4 │ Thermodynamics of $CO_2$ adsorption.** **a**, Isosteric heat of $CO_2$ adsorption plots for the mmen-$M_2$(dopbdc) series. **b**, Plot of the entropy of gaseous $CO_2$ against pressure at 298 K. **c**, A linear correlation was found to exist for each mmen-$M_2$(dopbdc) material between the step pressure at any temperature and the gas-phase entropy of $CO_2$, for mmen-$Mg_2$(dobpdc) (green, $R^2 = 0.99946$), mmen-$Mn_2$(dobpdc) (blue, $R^2 = 0.99918$), mmen-$Fe_2$(dobpdc) (orange, $R^2 = 0.99934$), mmen-$Co_2$(dobpdc) (purple, $R^2 = 0.99244$) and mmen-$Zn_2$(dobpdc) (black, $R^2 = 0.99932$).
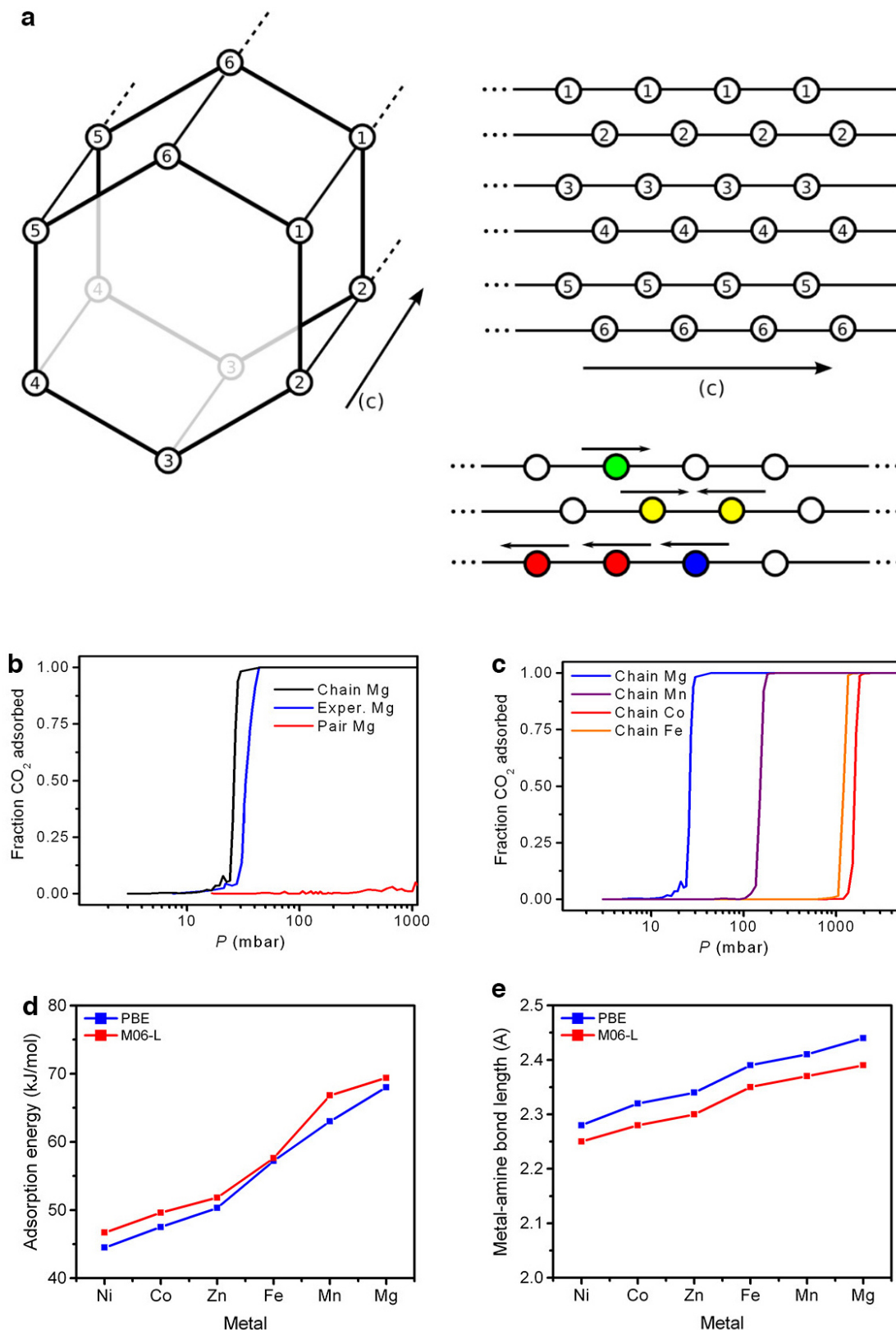
**Extended Data Figure 5 | Theoretical calculations. a**, Representation of the mapping of the hexagonal channel to a two-dimensional lattice in which each site consists of an amine that can interact with six neighbouring sites. Each amine can have one or zero $CO_2$ molecules adsorbed. A single site with a $CO_2$ adsorbed is shown in green. Pairs are allowed to form in both the crystallographic *c* direction and in the *a–b* plane (yellow); to model the chain mechanism, an amine in the middle of the chain is shown in red, and the amine at the end of the chain is in blue. **b**, Calculated $CO_2$ adsorption isotherms indicate that only a chain model of interactions rather than pairwise adsorption interactions can give rise to the experimentally stepped isotherm shape. **c**, On the basis of calculated adsorption enthalpies, the relative positions of adsorption isotherms can be predicted from the chain model. **d, e**, DFT calculations reflect the experimentally observed trend that $CO_2$ adsorption enthalpy (**d**) is related to the strength of the nitrogen-amine bond, as reflected by the calculated metal-amine bond length (**e**).
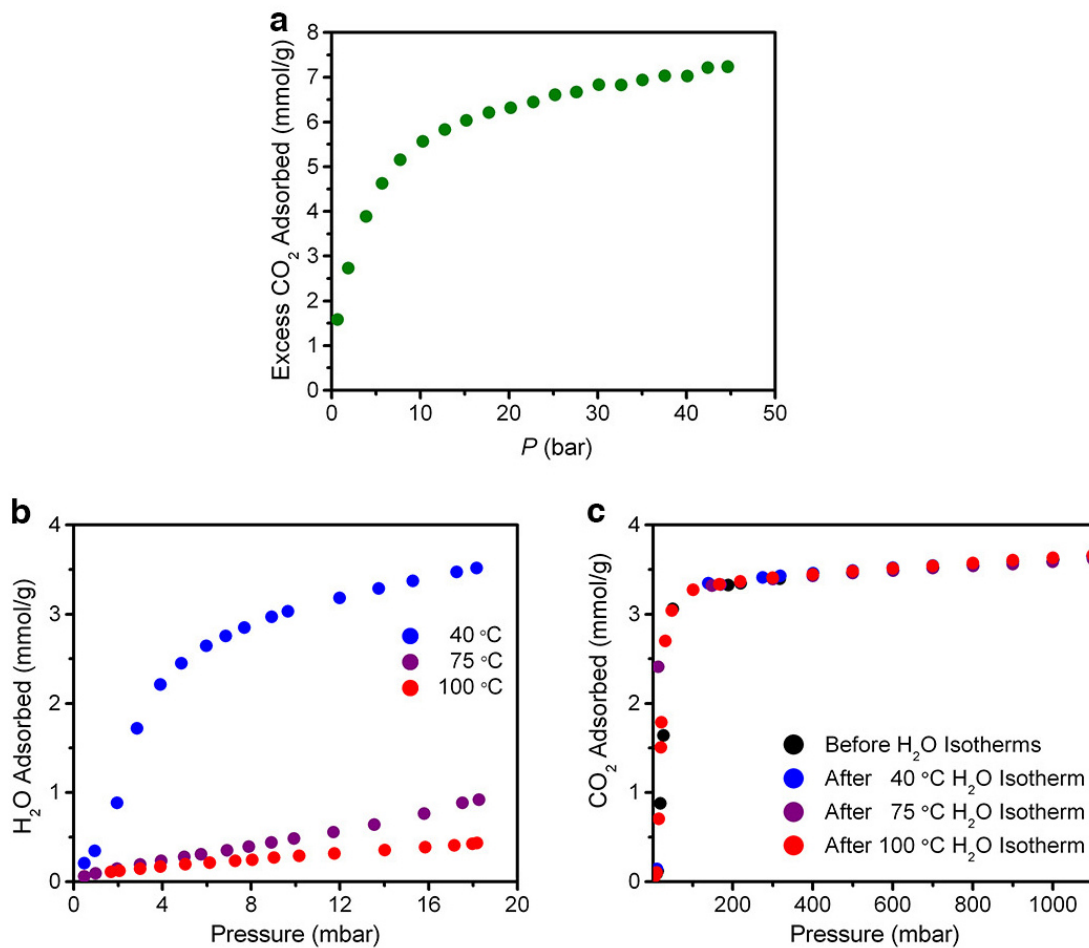
**Extended Data Figure 6 | Volumetric gas adsorption. a**, High-pressure excess $CO_2$ adsorption isotherm at 25 °C for mmen-Ni$_2$(dobpdc) indicates that Langmuir-type adsorption behaviour is maintained even at high pressures. **b**, Isothermal adsorption measurements of water onto a sample of mmen-Mg$_2$(dobpdc) at 40, 75 and 100 °C. **c**, Four isothermal adsorption measurements of $CO_2$ at 75 °C onto a sample of mmen-Mg$_2$(dobpdc) before exposure to water and after water isotherms at 40, 75 and 100 °C. No changes in the $CO_2$ adsorption isotherms were apparent from exposure of the sample to water.
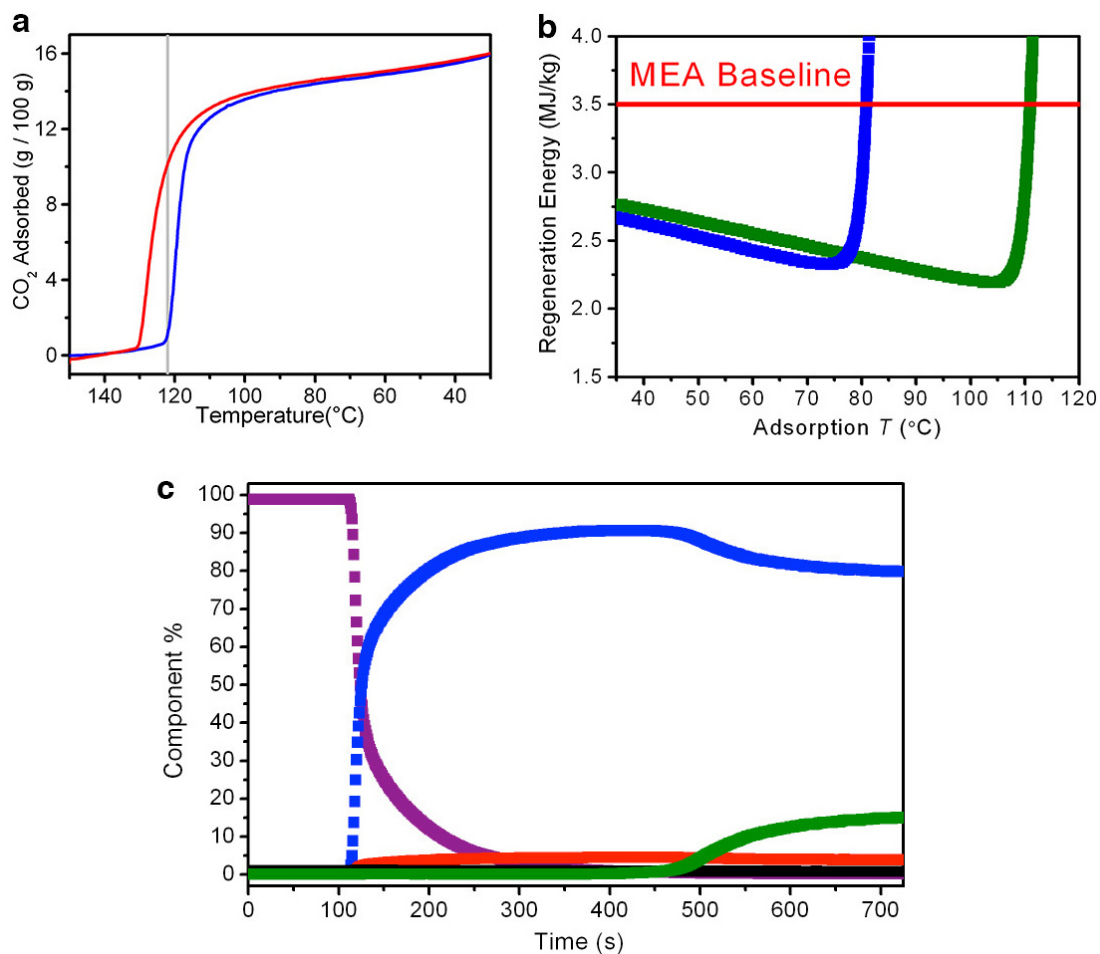
**Extended Data Figure 7 | Dynamic gas adsorption and regeneration energy.**
**a**, Isobaric, variable temperature (ramp rate of $1\,^{\circ}C\,min^{-1}$) gravimetric adsorption experiments for mmen-$Mg_2$(dobpdc) under 100% $CO_2$. Cooling from 150 to 30 °C is shown as the blue line, and heating from 30 to 150 °C as the red line. Desorption hysteresis was minimal because the phase-transition temperature and pressure are unchanged between adsorption and desorption. **b**, Regeneration energy calculations for mmen-$Mg_2$(dobpdc) (green) and mmen-$Mn_2$(dobpdc) (blue) indicate that effecting adsorption at high temperatures can be considerably more efficient than adsorption at 40 °C. **c**, Transient breakthrough of 15% $CO_2$ (green), 4% $O_2$ (red), 1.5% water (black) and balance $N_2$ (blue) through an adsorbent bed packed with mmen-$Mg_2$(dobpdc) at 25 °C. The adsorbent bed was under Ar (purple) before adsorption; a breakthrough $CO_2$ capacity of $2.7\,mmol\,g^{-1}$ was calculated.